Scientific Reports

https://doi.org/10.1038/s41598-026-44787-9

Article in Press

Mirrorless open cavities enabled by boundary incompatibility between perfect electric conductor and perfect magnetic conductor parallel-plate waveguides

Received: 19 January 2026

Accepted: 13 March 2026

Published online: 20 March 2026

Cite this article as: Kim S. & Kee C. Mirrorless open cavities enabled by boundary incompatibility between perfect electric conductor and perfect magnetic conductor parallel-plate waveguides. *Sci Rep* (2026). https://doi.org/10.1038/s41598-026-44787-9

Seong-Han Kim & Chul-Sik Kee

Mirrorless Open Cavities Enabled by Boundary Incompatibility between Perfect Electric Conductor and Perfect Magnetic Conductor Parallel-Plate Waveguides

Seong-Han Kim[1] **and Chul-Sik Kee**[1,*]

[1]Advanced Photonics Research Institute, Gwangju Institute of Science and Technology, Gwangju 61005, Republic of Korea
[*]corresponding author: cskee@gist.ac.kr

ABSTRACT

The most basic approach to confining electromagnetic waves is to place mirrors along their path, yet achieving confinement without conventional mirrors remains a major challenge. Here, we demonstrate theoretically and numerically an open-geometry cavity that enables electromagnetic field confinement without physical mirrors. This mirrorless confinement arises from a mode gap induced by incompatible boundary conditions at the interface between perfect electric conductor (PEC) and perfect magnetic conductor (PMC) parallel-plate waveguides. By employing a metallic-groove artificial magnetic conductor to emulate PMC behavior, we realize open PEC–PMC cavities that exhibit strong field localization and an enhanced magnetic-dipole Purcell factor. Waveguide-coupling simulations reveal a sharp transmission resonance with a quality factor of $Q \sim 10^2$, even in the presence of realistic Ohmic and dielectric losses. These mirrorless open cavities remove the physical boundaries imposed by conventional mirrors, allowing atoms, molecules, quantum dots, and biological nanoparticles to freely access and strongly couple to confined modes, thereby providing a versatile platform for exploring electromagnetic-wave phenomena in open geometries.

Introduction

The control of electromagnetic (EM) wave propagation through the utilization of frequency regions in which propagation is prohibited, referred to as mode gaps, is fundamental to a broad range of photonic systems. For example, in photonic crystals, periodic modulation of the refractive index gives rise to Bragg scattering and the formation of photonic band gaps, within which no Bloch modes can propagate.[1] In waveguides, cutoff conditions dictated by geometrical or material parameters suppress higher-order modes, resulting in waveguide mode gaps.[2] Metamaterials, on the other hand, employ subwavelength resonators to tailor the dispersion relation and introduce engineered gaps in the modal spectrum.[3] In all these systems, mode gaps emerge from structural periodicity, material dispersion, or geometrical design.

In contrast, the interface between semi-infinite perfect electric conductor (PEC) and perfect magnetic conductor (PMC) parallel-plate waveguides (PPWs) separated by an air gap h gives rise to a fundamentally distinct type of mode gap.[4] This effect originates solely from the incompatibility of boundary conditions. A PEC surface enforces the vanishing of the tangential electric field and reflects incident waves with a phase shift of π, whereas a PMC surface enforces the vanishing of the tangential magnetic field and reflects with zero phase shift.[5] For time-harmonic fields ($e^{-i\omega t}$), these boundary conditions are expressed as $\hat{\mathbf{n}} \times \mathbf{E} = \mathbf{0}$ for a PEC surface and $\hat{\mathbf{n}} \times \mathbf{H} = \mathbf{0}$ for a PMC surface, where $\mathbf{E}$ and $\mathbf{H}$ denote the electric and magnetic fields, respectively, and $\hat{\mathbf{n}}$ is the unit normal vector perpendicular to the surface.

When two PEC plates form a parallel-plate waveguide (PPW) with separation $h < \lambda/2$, only the TEM mode can propagate. In contrast, a PMC PPW supports a complementary TEM mode in which the roles of the electric and magnetic fields are interchanged. If a PEC PPW and a PMC PPW are connected side by side, the interface between them imposes mutually incompatible constraints on the tangential field components for any TEM-like solution across the junction. As a consequence, propagating transmission is suppressed below the first cutoff frequency, $f_{\text{cutoff}} = c/2h$ and the interface effectively behaves as a reflecting boundary. This reflection does not arise from material index contrast but from boundary-condition incompatibility, forming a virtual electric wall even in the absence of a physical mirror.

Building on this boundary incompatibility, a rich variety of unconventional electromagnetic phenomena has been revealed. PEC–PMC interfaces can sustain surface waves even in media with positive permittivity and permeability, defying the

conventional requirement for negative material parameters and exhibiting plasmon-like resonances in cylindrical geometries.[6] A circular PMC patch embedded in a PEC PPW behaves as a virtual pillar, completely shielding an enclosed object while allowing controlled field penetration determined by pillar height.[7] Periodic arrays of such virtual pillars reproduce the band structures of metallic photonic crystals, exhibiting photonic band gaps, double Dirac cones, and effective zero-index behavior.[8] Likewise, alternating PEC and PMC PPWs filled with dielectric layers support hyperbolic dispersion and negative refraction, analogous to metal-dielectric multilayers,[9] although similar phenomena can also be realized using PEC PPWs alone in the absence of the PMC boundary.[10–12] Interfacing Weyl photonic metamaterials with PEC or PMC boundaries enables all-angle reflectionless negative refraction,[13] and a finite-thickness photonic meta-crystal subjected to these boundary conditions exhibits opposite chiral bulk transport.[14] The EM field enhancement for the scattering of a plane wave by a subwavelength rectangular cavity formed by PEC walls and a PMC bottom has been reported.[15]

This boundary incompatibility enables the formation of mirrorless open EM cavities confined not by physical walls but by virtual electric or magnetic barriers at the PEC–PMC interfaces. The term *"mirrorless"* emphasizes that no material mirrors enclose the cavity volume, even though reflection arises from the induced virtual electric or magnetic barriers. Although an ideal PMC does not exist in nature, its boundary behavior can be emulated by an artificial magnetic conductor (AMC), such as a high-impedance or frequency-selective surface, that reflects EM waves with near-zero phase shift over a narrow frequency band.[16–18] When integrated into PPW geometries, these engineered structures enable the realization of open EM cavities based on the mode gap arising from incompatible boundary conditions at the interface between PEC and PMC PPWs separated by an air gap.

In this paper, we theoretically and numerically demonstrate that EM waves can be confined by virtual electric or magnetic barriers formed by enclosing a PEC–PMC interface. To validate this confinement mechanism, rectangular PEC patches were implemented on the top and bottom plates of an AMC PPW separated by an air gap, where the AMC—realized using metallic grooves—emulates the behavior of a PMC. This configuration forms virtual electric walls via closed PEC–AMC interfaces, trapping EM energy within the air region between the patches. The quality factor Q of the lossless open cavity increases markedly as the gap h decreases, whereas in the presence of Ohmic and dielectric losses, Q is strongly suppressed and becomes nearly independent of h. Full-wave simulations based on evanescent-wave coupling confirm strong EM energy localization within the air region, despite the absence of any physical enclosure.

Results

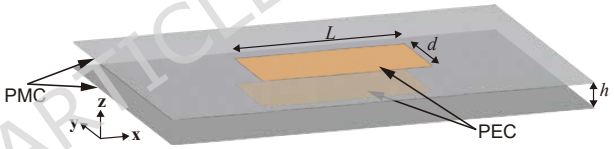

Figure 1. Schematic of an open EM cavity formed by virtual electric walls at the interfaces between two rectangular PEC patches of size $L \times d$ and a PMC parallel-plate waveguide separated by an air gap h, with the patches embedded in the top and bottom plates.

Figure 1 schematically illustrates an open EM cavity formed by virtual electric walls at the interfaces between two rectangular PEC patches of size $L \times d$ ($-L/2 \le x \le L/2$, $-d/2 \le y \le d/2$) and a PMC PPW separated by an air gap h ($0 \le z \le h$), with the patches embedded in the top and bottom plates. An equivalent structure with PMC patches in a PEC PPW supports identical mode solutions when the electric and magnetic field components are interchanged.

For PEC patches of size $L \times d$ embedded in an ideal PMC PPW separated by an air gap h, the frequencies of the cavity modes confined within the air gap between the top and bottom patches are given by $f_c = c\sqrt{(p/L)^2 + (q/d)^2}/2$, where p and q are integers below the first cutoff frequency $f_{\text{cutoff}} = c/2h$. The fundamental cavity mode corresponds to $p = 1$ and $q = 0$, yielding $f_c = c/2L$ for $d < L$, and supports only the z-component of the electric field, $E_z = E_0 \sin(\pi x/L)$, and the y-component of the magnetic field, $H_y = H_0 \cos(\pi x/L)$.

Figures 2(a) and 2(b) show the spatial distributions of the electric field component E_z and magnetic field component H_y, respectively. For each field component, the upper panel displays the xy-plane distribution at $z = h/2$, and the lower panel shows the xz-plane distribution at $y = 0$. The cavity mode at $f_c = 25.33$ GHz is confined in the air region between PEC patches of size $6a \times 2a$ embedded in the PMC PPW with $h = a = 1.0$ mm. The simulated field profiles of E_z and H_y agree well with the analytical solutions, $E_z = E_0 \sin(\pi x/L)$ and $H_y = H_0 \cos(\pi x/L)$ and clearly demonstrate strong EM energy confinement in the air region, even without any physical enclosure.

In practical implementation, a PMC can be emulated by an AMC, which requires a sufficient number of unit cells to reproduce PMC-like behavior; AMC patches with too few unit cells deviate from the ideal. Here, we study the PEC-patch/AMC

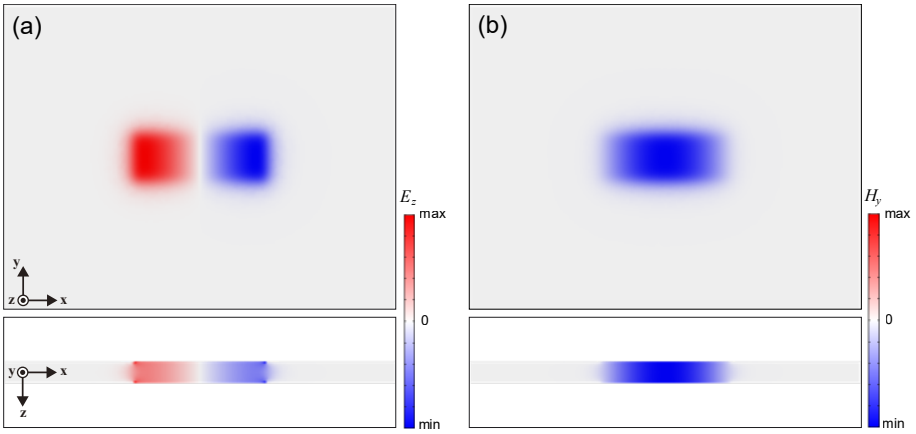

Figure 2. Spatial distributions of the electric field component E_z in the xy plane at $z = h/2$ (upper panel) and the xz plane at $y = 0$ (lower panel) (a), and of the magnetic field component H_y in the xy plane at $z = h/2$ (upper panel) and the xz plane at $y = 0$ (lower panel) (b), for the cavity mode ($f_c = 25.33$ GHz) confined in the air region between PEC patches of size $6a \times 2a$ embedded in the PMC PPW with $h = a = 1.0$ mm.

PPW configuration, where virtual electric walls confine the fields in the air gap between the patches. Figure 3(a) shows the schematic of a metallic-groove AMC, composed of a two-dimensional array of square metal rods on a flat metal surface within a dielectric background of refractive index n_d. The array period is a, while b and t denote the rod width and height, respectively. This AMC design is employed because it integrates seamlessly with PEC patches and establishes a well-defined PEC–AMC boundary interface.[6]

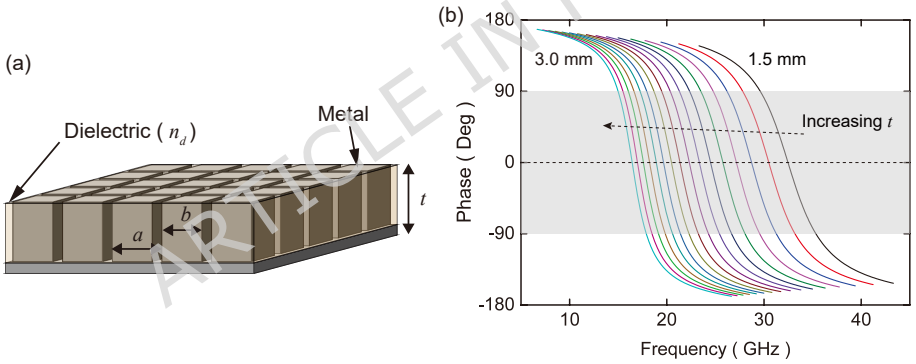

Figure 3. (a) Schematic of a metallic-groove AMC, consisting of a two-dimensional array of square metal rods on a flat metal surface within a dielectric background of refractive index n_d. The array period is a, while b and t denote the rod width and height, respectively. (b) Reflection phase of normally incident EM waves on the metallic groove structure for $a = 1.0$ mm, $b = 0.8a$, and $n_d = 1.5$, with t varied from 1.5 to 3.0 mm. The structure functions as an AMC within the frequency range where the reflection phase lies between $+90°$ and $-90°$, highlighted in gray.

Figure 3(b) shows the reflection phase of normally incident EM waves on the artificial structure, with t varied from 1.5 to 3.0 mm, $a = 1.0$ mm, $b = 0.8a$, and $n_d = 1.5$. The structure acts as a magnetic conductor within the frequency range where the reflection phase lies between $+90°$ and $-90°$, highlighted in gray.[18] An approximate expression for the zero-phase frequency, $f_{\varphi=0}$, is $c/\left(4tn_{\varphi=0}\right)$, where c is the speed of light in free space and $n_{\varphi=0}$ is the effective refractive index at the zero-phase frequency. The EM field confinement within the PEC–patch/AMC PPW is examined at this zero-phase frequency.

At the boundary of semi-infinite PEC/PMC PPWs, the virtual electric wall enforces incompatible boundary conditions that yield perfect reflection. In a PEC–patch/PMC PPW cavity, however, the finite dimensions of the PEC patches and the PMC PPW lead to imperfect reflection, allowing the cavity mode to leak through evanescent field tails beyond the patch region. As h decreases, the reflectivity of the virtual electric wall increases;[7,8] thus, larger h effectively extends the cavity length and lowers the cavity frequency below $c/2L$. When PEC patches of the same size are embedded in a metallic-groove AMC PPW, the fundamental cavity frequency can be tuned to match the zero-phase frequency by adjusting t. In this configuration, the AMC effectively mimics a PMC, and the spatial distributions of E_z and H_y closely resemble those of the PEC–patch/PMC PPW case.

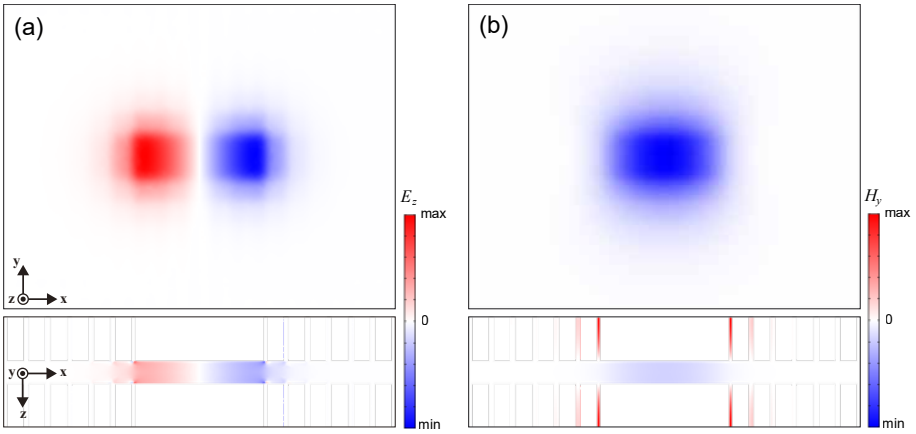

Figure 4. Spatial distributions of the electric field component E_z in the xy plane at $z = h/2$ (upper panel) and the xz plane at $y = 0.5a$ (lower panel) (a), and of the magnetic field component H_y in the xy plane at $z = h/2$ (upper panel) and the xz plane at $y = 0.5a$ (lower panel) (b), for the cavity mode ($f_c = 25.47$ GHz) confined in the air region between PEC patches of size $6a \times 2a$ embedded in the metallic-groove AMC PPW of size $18a \times 14a$, with $t = 2.0$ mm and $h = a = 1.0$ mm. The fields resemble the PEC–patch/PMC PPW fundamental mode, confirming open-geometry confinement in the xy plane.

Figures 4(a) and 4(b) show the spatial distributions of the electric field component E_z and the magnetic field component H_y, respectively, in the xy plane at $z = h/2$ (upper panels) and in the xz plane at $y = 0$ (lower panels) for the cavity mode confined in the air region between PEC patches ($6a \times 2a$) embedded in a metallic-groove AMC PPW of size $18a \times 14a$, with $t = 2.0$ mm and $h = a = 1.0$ mm. The simulated field patterns closely resemble those of the fundamental mode in the PEC-patch/PMC PPW case shown in Figs. 2(a) and 2(b), confirming that the virtual electric walls formed by the boundary-incompatibility-induced mode gap effectively confine the EM field without physical enclosures. These results verify that the PEC-patch/AMC PPW operates as an open EM cavity.

A key implication of the open cavity formed by PEC–patch/AMC PPWs is its ability to enhance light–matter interactions through the Purcell effect.[19] The virtual electric wall created by incompatible boundary conditions enables strong confinement of the cavity mode within the air region between the PEC patches, resulting in a small effective mode volume. When combined with the high quality factor achievable in the absence of significant material losses, this confinement leads to a substantial enhancement of the spontaneous emission rate of a magnetic dipole emitter placed inside the cavity.

In a PEC–patch/PMC PPW open cavity with $\mathbf{H} = H_0 \cos(\pi x/L)\hat{\mathbf{y}}$, the magnetic-dipole Purcell factor is given by $F_{P,\mathrm{MD}} = (3/4\pi^2)(\lambda/n)^3 Q/V_{\mathrm{MD}}\, \eta_{\mathrm{pos}}\, \eta_{\mathrm{ori}}\, \eta_{\mathrm{spec}}$, where λ is the free-space wavelength, n is the refractive index, Q is the cavity quality factor, and the effective mode volume is defined as $V_{\mathrm{MD}} = \int |\mathbf{H}|^2 d^3r / \max|\mathbf{H}|^2 = Ldh/2$. The correction factors $\eta_{\mathrm{pos}} = \cos^2(\pi x_0/L)$, $\eta_{\mathrm{ori}} = (\hat{\mathbf{m}} \cdot \hat{\mathbf{H}})^2$, and η_{spec} describe the emitter position, dipole orientation, and spectral detuning, respectively, where x_0 denotes the position of a magnetic dipole emitter and $\hat{\mathbf{m}}$ its magnetic dipole moment.[20,21]

For an optimally placed emitter at the antinode ($x_0 = 0$) and aligned on resonance, the Purcell factor reduces to $F_{P,\mathrm{MD}} = (12/\pi^2)(L^2/dh)Q$ for $\lambda = 2L$ and $n = 1$, demonstrating strong spontaneous-emission enhancement that scales quadratically with L, inversely with d and h, and linearly with Q. In the PEC–patch/AMC PPW open cavity, where the field profile closely resembles that of the ideal PEC–patch/PMC PPW case, the Purcell factor is given by $F_{P,\mathrm{MD}} = (12/\pi^2)(L^2/\gamma dh)Q$ for an optimally placed emitter, with $\gamma > 1$ accounting for finite field leakage.

The quality factor (Q) is determined by the reflectivity R of the virtual electric walls, with $Q \sim 1/(1-R)$. Consequently, Q increases as h decreases or as the relative size of the AMC PPW compared to the PEC patch increases, since the reflectivity R rises under these conditions.[7,8] Therefore, h is a key parameter for enhancing the Purcell factor of the fundamental cavity mode in the PEC-patch/AMC PPW open cavity. As h is reduced, $F_{P,\mathrm{MD}}$ increases significantly.

Figure 5 shows the dependence of Q of the PEC–patch/AMC PPW open cavity on h. Under lossless conditions, Q rises rapidly with decreasing h due to stronger field confinement. In the presence of Ohmic dissipation in copper with conductivity $\sigma = 5.813 \times 10^7$ S/m and dielectric losses with a loss tangent of 0.0009, however, Q is strongly suppressed and becomes nearly independent of h, saturating at values of order 10^2. The total loss α_t is the sum of radiative loss α_r and material loss α_m ($\alpha_t = \alpha_r + \alpha_m$), with Q inversely proportional to loss ($1/Q_t = 1/Q_r + 1/Q_m$). In the lossy case, $\alpha_r \ll \alpha_m$ so that $\alpha_t \approx \alpha_m$ and $Q_t \approx Q_m$, independent of h. This limitation caps the magnetic-dipole Purcell factor at $\sim 10^3$ and highlights the critical role of loss mitigation in practical implementations.

The Ohmic loss in the metal is governed by the surface resistance $\sqrt{\omega\mu_0/2\sigma}$, which follows from the skin-depth

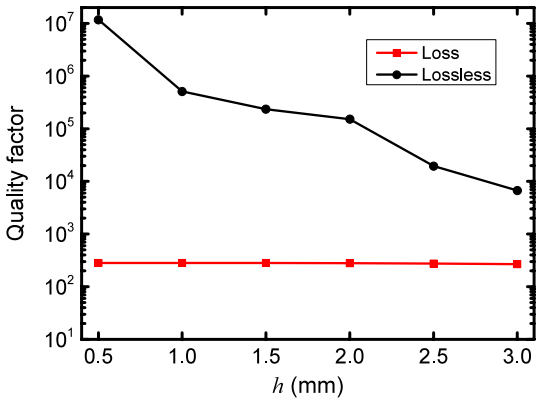

Figure 5. Dependence of the quality factor on h.

approximation for good conductors.[5] Since the Ohmic-loss-limited quality factor scales inversely with the surface resistance, $Q \propto \sqrt{\sigma}$, a metal with higher conductivity yields a modest increase in Q. For example, Ag, having slightly higher conductivity than Cu, would therefore provide a somewhat larger Q.

To examine the device potential of the PEC–patch/AMC PPW open cavity, we perform a numerical waveguide-coupling experiment by placing two finite PEC PPWs adjacent to the cavity, as schematically illustrated in the inset of Fig. 6(a). In a waveguide–resonator system with two parallel waveguides, the output response is governed by the resonator mode: a single even mode produces bidirectional outputs in both waveguides irrespective of the input port, whereas a single odd mode yields output characteristics determined by the waveguide configuration[22]. The input–output configuration is optimized to ensure sufficient transmission by efficiently coupling the odd-parity electric field to the waveguide modes.

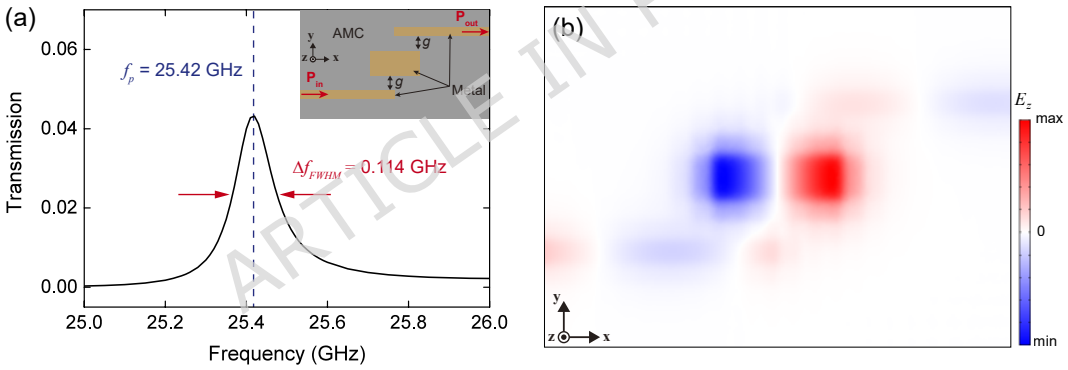

Figure 6. (a) Simulated transmission spectrum of TEM modes in the side-coupled PEC PPW of width a within the AMC PPW of size $22a \times 16a$ containing a PEC–patch/AMC PPW open cavity of size $6a \times 2a$. The waveguide–cavity separation is $g = 2a$. The inset shows a schematic of the numerical waveguide-coupling experiment. (b) Spatial distribution of E_z in the xy plane at $z = h/2$ for the peak frequency of the transmission spectrum.

Figure 6(a) shows the simulated transmission spectra of TEM modes in the side-coupled PEC PPW of width a embedded in an AMC PPW of size $22a \times 16a$ containing a PEC–patch/AMC PPW open cavity of size $6a \times 2a$. The waveguide–cavity separation is $g = 2a$, with an air-gap height of $h = a = 1.0$ mm. The spectrum exhibits a sharp peak at the fundamental frequency near 25.4 GHz. The estimated $Q = f_p/\Delta f_{\mathrm{FWHM}}$ is on the order of 10^2, in good agreement with the calculated Q for the lossy case in Fig. 5, where f_p is the peak frequency and Δf_{FWHM} is the full width at half maximum.

The low peak transmission originates from the fact that the cavity operates in the regime, where intrinsic material loss dominates over external waveguide coupling. Within temporal coupled-mode theory,[23] the cavity amplitude $a(t)$ satisfies $da/dt = (i\omega_0 - \gamma_i - \gamma_e)\,a + \sqrt{2\gamma_e}\,s_{\mathrm{in}}$, where γ_i denotes the intrinsic loss rate (Ohmic and dielectric losses), and γ_e denotes the external coupling rate to the waveguide. Here s_{in} denotes the incoming wave amplitude from the excitation port, normalized such that $|s_{\mathrm{in}}|^2$ corresponds to the input power. The transmission spectrum is given by $T(\omega) = 4\gamma_e^2/[(\omega - \omega_0)^2 + (\gamma_i + \gamma_e)^2]$. At resonance ($\omega = \omega_0$), the peak transmission reduces to $T_{\max} = 4\gamma_e^2/(\gamma_i + \gamma_e)^2$. In the present configuration, strong field confinement enhances Ohmic dissipation, leading to $\gamma_i \gg \gamma_e$ ($\alpha_m \gg \alpha_r$). Consequently, $T_{\max} \approx 4\gamma_e^2/\gamma_i^2 \ll 1$, which explains the low transmission peak observed in Fig. 6(a). In addition to the intrinsic material loss discussed above, another factor

contributing to the low transmission is the mode mismatch between the plane waves incident from (and radiating to) the external region and the guided modes of the input and output PEC waveguides. This mismatch reduces the coupling efficiency between the external excitation and the waveguide modes, leading to additional input and output losses and consequently lowering the overall transmission.

Figure 6(b) displays the spatial distribution of E_z in the xy plane at $z = h/2$ for the peak frequency. The side-coupled PEC PPWs act as open waveguides, with virtual electric walls induced by boundary incompatibility confining the EM field in the air region without physical enclosure, analogous to an open cavity. Since the coupling properties between an open cavity and an open waveguide are essentially the same as those of a conventional resonator–waveguide system, a variety of conventional devices can be implemented within an AMC PPW by replacing the resonators and waveguides with open cavities and open waveguides.

In practical microwave implementations, the challenges are predominantly technical rather than conceptual. The AMC exhibits PMC-like behavior only within a finite bandwidth around its zero-phase frequency, which requires precise control of structural parameters, particularly the groove height t. Fabrication tolerances can shift the zero-phase frequency and weaken the effective magnetic-boundary response. In addition, intrinsic material losses-including Ohmic loss in the metal and dielectric loss in the substrate-significantly limit the achievable quality factor, as confirmed by our lossy simulations. A sufficiently large number of AMC unit cells is also necessary to approximate ideal PMC behavior, since finite-size effects reduce effective reflectivity and thereby weaken field confinement.

Beyond the microwave regime, scaling the present concept to terahertz frequencies is, in principle, feasible through geometric scaling of the AMC structure. However, at higher frequencies, metal dispersion and increased loss become increasingly significant, potentially reducing the attainable quality factor. In the optical regime, realizing low-loss PMC-like boundary conditions becomes more challenging due to plasmonic dissipation in metals and the limited bandwidth of artificial magnetic responses. Nevertheless, alternative implementations based on dielectric resonator arrays or all-dielectric metamaterials may provide viable pathways for extending boundary-incompatibility-induced confinement beyond microwave frequencies. These considerations suggest that while practical performance is presently loss-limited, the underlying confinement mechanism remains broadly applicable across frequency scales.

A distinctive advantage of the proposed open cavity is the absence of physical boundaries imposed by conventional mirrors. This geometry allows atoms, molecules, magnetic quantum dots only a few nanometers in size, and even biological species such as viruses to freely enter the cavity region and strongly interact with the confined electromagnetic fields. Such accessibility creates unprecedented opportunities for exploring strong light–matter coupling, magnetically mediated interactions, and cavity quantum electrodynamics in open environments that are difficult to realize with conventional closed cavities. This boundary-incompatibility-induced mirrorless confinement is expected to stimulate new interdisciplinary research in photonics, quantum science, and bio-integrated cavity systems.

Conclusion

In summary, we have introduced a new confinement mechanism for EM waves based on boundary-incompatibility-induced mode gaps at PEC–PMC interfaces, enabling open cavities bounded by virtual electric or magnetic walls without physical mirrors. By implementing metallic-groove AMCs, we demonstrated PEC–patch/AMC PPW open cavities and verified their confinement properties through full-wave simulations and a numerical waveguide-coupling experiment. The simulations reveal strong localization with an enhanced magnetic-dipole Purcell factor, while the experiment confirms a sharp transmission peak with $Q \sim 10^2$ under realistic Ohmic and dielectric losses. These results establish a general strategy for mirrorless EM field confinement and open new avenues for photonic, quantum, and bio-integrated cavity systems.

Numerical method

All simulations were performed using the finite-element method implemented in COMSOL Multiphysics. For resonators surrounded by PMC (AMC), complex eigenfrequencies were obtained using the eigenfrequency study with a tetrahedral mesh. The maximum mesh element size was set to approximately $\lambda/20$, providing reliable numerical convergence while maintaining a reasonable computational cost. Perfectly matched layers were applied at the boundaries to model open radiation conditions. Transmission spectra for waveguide coupling were calculated using the frequency-domain solver with a frequency sweep.

Competing interests

The authors declare that there are no competing interests.

Funding

This work was supported by the National Research Foundation of Korea grant funded by the Korea government (Ministry of Science, Information and Technology) (RS-2024-00449337) and the Future-Leading Specialized Research Project grant funded by Gwangju Institute of Science and Technology in 2026.

Author contributions statement

C. -S. Kee wrote the main manuscript text. S. -H. Kim performed numerical simulations and prepared all figures. All authors reviewed the manuscript.

Data availability

The datasets used and/or analysed during the current study available from the corresponding author on reasonable request.

References

1. Joannopoulos, J. D., Johnson, S. G., Winn, J. N. & Meade, R. D. *Photonic Crystals: Molding the Flow of Light - Second Edition* (Princeton University Press, 2011).
2. Mahmoud, S. F. *Electromagnetic Waveguides: Theory and applications* (The Institution of Engineering and Technology, 1991).
3. Cai, W. & Shalaev, V. *Optical Metamaterials: Fundamentals and Applications* (Springer New York, 2009).
4. Li, D. C., Boone, F., Bozzi, M., Perregrini, L. & Wu, K. Concept of virtual electric/magnetic walls and its realization with artificial magnetic conductor technique. *IEEE Microw. Wirel. Components Lett.* **18**, 743–745, DOI: 10.1109/LMWC.2008.2005229 (2008).
5. Pozar, D. M. *Microwave Engineering*, vol. 2 (Wiley, New York, 1998).
6. Kim, S.-H. & Kee, C.-S. Discovery of electromagnetic surface waves at the interface between perfect electric conductor and perfect magnetic conductor parallel-plate waveguides. *Phys. Rev. Lett.* **133**, 186901, DOI: 10.1103/PhysRevLett.133.186901 (2024).
7. Kim, S.-H. & Kee, C.-S. Electromagnetic shielding via a virtual pillar with a magnetic wall. *Results Phys.* **14**, 102462, DOI: https://doi.org/10.1016/j.rinp.2019.102462 (2019).
8. Kim, S.-H., Kim, S. & Kee, C.-S. Photonic crystals composed of virtual pillars with magnetic walls: Photonic band gaps and double dirac cones. *Phys. Rev. B* **94**, 085118, DOI: 10.1103/PhysRevB.94.085118 (2016).
9. Kim, S.-H. & Kee, C.-S. Hyperbolic dispersion and negative refraction in a periodic perfect magnetic conductor and perfect electric conductor parallel-plate waveguide structure. *Results Phys.* **77**, 108459, DOI: https://doi.org/10.1016/j.rinp.2025.108459 (2025).
10. Ji, W. *et al.* Cladding-free hyperbolic waveguide arrays. *ACS Photonics* **11**, 2422–2429, DOI: 10.1021/acsphotonics.4c00308 (2024). https://doi.org/10.1021/acsphotonics.4c00308.
11. Ji, W., Zhou, X., Chu, H., Luo, J. & Lai, Y. Theory and experimental observation of hyperbolic media based on structural dispersions. *Phys. Rev. Mater.* **4**, 105202, DOI: 10.1103/PhysRevMaterials.4.105202 (2020).
12. Ji, W., Luo, J. & Lai, Y. Extremely anisotropic epsilon-near-zero media in waveguide metamaterials. *Opt. Express* **27**, 19463–19473, DOI: 10.1364/OE.27.019463 (2019).
13. Liu, Y., Wang, G. P., Pendry, J. B. & Zhang, S. All-angle reflectionless negative refraction with ideal photonic weyl metamaterials. *Light. Sci. & Appl.* **11**, 276, DOI: 10.1038/s41377-022-00972-9 (2022).
14. Qi, Y., Wang, H., Guo, Q., Zhu, Z. & Yang, B. Photonic chiral bulk transports manipulated by boundary freedom in three-dimensional meta-crystals. *ACS Photonics* **12**, 4494–4502, DOI: 10.1021/acsphotonics.5c00870 (2025). https://doi.org/10.1021/acsphotonics.5c00870.
15. Gao, P., Y. Li & Yuan, X. Electromagnetic field enhancement in a subwavelength rectangular open cavity. *Partial. Differ. Equ. Appl.* **2**, DOI: https://doi.org/10.1007/s42985-021-00108-5 (2021).
16. Sievenpiper, D., Zhang, L., Broas, R., Alexopolous, N. & Yablonovitch, E. High-impedance electromagnetic surfaces with a forbidden frequency band. *IEEE Transactions on Microw. Theory Tech.* **47**, 2059–2074, DOI: 10.1109/22.798001 (1999).

17. Ma, K.-P., Hirose, K., Yang, F.-R., Qian, Y. & Itoh, T. Realisation of magnetic conducting surface using novel photonic bandgap structure. *Electron. Lett.* **34**, 2041–2042, DOI: 10.1049/el:19981391 (1998).

18. Hadarig, R. C., de Cos, M. E. & Las-Heras, F. Novel miniaturized artificial magnetic conductor. *IEEE Antennas Wirel. Propag. Lett.* **12**, 174–177, DOI: 10.1109/LAWP.2013.2245093 (2013).

19. Purcell, E. M. Spontaneous emission probabilities at radio frequencies. *Phys. Rev.* **69**, 681 (1946).

20. Koenderink, A. F. On the use of purcell factors for plasmon antennas. *Opt. Lett.* **35**, 4208–4210, DOI: 10.1364/OL.35.004208 (2010).

21. Baranov, D. G., Savelev, R. S., Li, S. V., Krasnok, A. E. & Alù, A. Modifying magnetic dipole spontaneous emission with nanophotonic structures. *Laser & Photonics Rev.* **11**, 1600268, DOI: https://doi.org/10.1002/lpor.201600268 (2017).

22. Fan, S. *et al.* Theoretical analysis of channel drop tunneling processes. *Phys. Rev. B* **59**, 15882–15892, DOI: 10.1103/PhysRevB.59.15882 (1999).

23. Fan, S., Suh, W. & Joannopoulos, J. D. Temporal coupled-mode theory for the fano resonance in optical resonators. *J. Opt. Soc. Am. A* **20**, 569–572, DOI: 10.1364/JOSAA.20.000569 (2003).